



# Coupling a Global Heliospheric Magnetohydrodynamic Model to a Magnetofrictional Model of the Low Corona

Keiji Hayashi<sup>1</sup> , William P. Abbett<sup>2</sup> , Mark C. M. Cheung<sup>3</sup> , and George H. Fisher<sup>2</sup>

<sup>1</sup> W. W. Hansen Experimental Physics Laboratory, Stanford University, Stanford, CA 94305, USA; [keiji@sun.stanford.edu](mailto:keiji@sun.stanford.edu)

<sup>2</sup> Space Sciences Laboratory, University of California, 7 Gauss Way, Berkeley, CA 94720-7450, USA

<sup>3</sup> Lockheed Martin Solar and Astrophysics Laboratory, Building 252, 3251 Hanover Street, Palo Alto, CA 94304, USA

Received 2020 December 12; revised 2021 February 22; accepted 2021 February 23; published 2021 April 19

## Abstract

Recent efforts coupling our Sun-to-Earth magnetohydrodynamics (MHD) model and lower-corona magnetofrictional (MF) model are described. Our Global Heliospheric MHD (GHM) model uses time-dependent three-component magnetic field data from the lower-corona MF model as time-dependent boundary values. The MF model uses data-assimilation techniques to introduce the vector magnetic field data from the Solar Dynamics Observatory/Helioseismic and Magnetic Imager, hence as a whole this simulation coupling structure is driven with actual observations. The GHM model employs a newly developed interface boundary treatment that is based on the concept of characteristics, and it properly treats the interface boundary sphere set at a height of the sub-Alfvénic lower corona ( $1.15 R_{\odot}$  in this work). The coupled model framework numerically produces twisted nonpotential magnetic features and consequent eruption events in the solar corona in response to the time-dependent boundary values. The combination of our two originally independently developed models presented here is a model framework toward achieving further capabilities of modeling the nonlinear time-dependent nature of magnetic field and plasma, from small-scale solar active regions to large-scale solar wind structures. This work is a part of the Coronal Global Evolutionary Model project for enhancing our understanding of Sun–Earth physics to help improve space weather capabilities.

*Unified Astronomy Thesaurus concepts:* [Solar corona \(1483\)](#); [Solar wind \(1534\)](#); [Magnetohydrodynamics \(1964\)](#); [Magnetohydrodynamical simulations \(1966\)](#)

## 1. Introduction

The Coronal Global Evolutionary Model (CGEM; Fisher et al. 2015; Hoeksema et al. 2020) is a model infrastructure framework capable of utilizing solar-surface three-component magnetic field data from the Helioseismic and Magnetic Imager on the Solar Dynamics Observatory (SDO/HMI; Scherrer et al. 2012; Hoeksema et al. 2014), estimating the solar-surface magnetic forces and energy fluxes, and simulating and reproducing nonpotential highly twisted coronal magnetic field features over a broad range of heliocentric distances from the solar surface to interplanetary space. The PDFI (PTD-Doppler-FLCT Ideal) method (e.g., Kazachenko et al. 2014; Fisher et al. 2020) is used to infer the solar-surface magnetic forces and electric field matching the observed temporal evolution of the magnetic field (Hoeksema et al. 2020).

The magnetofrictional (MF) model (e.g., Craig & Sneyd 1986; Yang et al. 1986; van Ballegoijen et al. 2000) and MHD models are powerful methods to simulate temporal evolution of the coronal magnetic field matching the observations. In the CGEM framework, the MF (Cheung & DeRosa 2012) and the RADMHD model (Abbett 2007; Abbett & Fisher 2012; Abbett & Bercik 2014) can numerically reproduce the coronal evolution in response to solar-surface magnetic field variations (Sections 4–6 of Hoeksema et al. 2020). In these models, however, the computation domain must often be limited to the lower corona, typically up to at most  $2.5 R_{\odot}$ , to avoid the computational difficulties at and beyond the Alfvén radius (at typically  $3 \sim 20 R_{\odot}$ ) or the critical radius of the Parker solution (at about  $5.5 R_{\odot}$  with the specific heat ratio  $\gamma \sim 1$ ).

To help enhance our capability in space weather studies, it is desirable to extend these near-Sun models driven by advanced

recent observations to the orbit of Earth at 1 au and beyond. A straightforward tactic for this domain extension is to apply output information from a lower coronal model to another solar-corona/solar-wind model (e.g., Steinolfson et al. 1982; Linker et al. 1990, 1999; Usmanov 1993; Feng et al. 2010, 2015, 2017; Riley et al. 2011; Usmanov et al. 2011; Jin et al. 2017), or a solar-wind model (e.g., Dryer et al. 1991; Odstrcil & Pizzo 1999, 2009; Detman et al. 2011; Wu et al. 2011; Hayashi 2012; Shen et al. 2013; Shiota & Kataoka 2016; Pogorelov et al. 2017; Pogano et al. 2018; Pomoell & Poedts 2018; Xiong et al. 2018; Hinterreiter et al. 2019; Li et al. 2020). A few other practical advantages are expected to result from this model coupling tactic: it will be far easier to fine-tune each model independently; the required computational resources will be substantially reduced compared to the case where two or more models are fully integrated into a single model code, and/or a single model handles the whole region of interest, from the solar corona to interplanetary space, with a vast magnitude range of temporal and spatial scales.

In this context, we have developed a new version of a Sun-to-Earth MHD model, named the Global Heliospheric MHD model (GHM) in the CGEM model framework (Section 7 of Hoeksema et al. 2020), by modifying our existing MHD models (Hayashi 2005, 2008, 2013; Hayashi et al. 2015). A new feature in the Sun-to-Earth GHM model is a set of boundary treatments for an interface boundary sphere to introduce the outputs from the lower-corona MF model as time-dependent boundary values to drive the upper corona and solar wind. In developing the new interface boundary treatment in the CGEM context, there are two requirements as described below.

The first requirement is that the interface is placed in the lower corona. As shown in Merkin et al. (2016), Pogano et al. (2018), and Li et al. (2020), the combination of two models is indeed powerful, capable of reproducing temporal variations of the plasma and magnetic field in the broader temporal scale and spatial range than each model can. These model combinations use two of the same or similar MHD models and have the interface at the super-Alfvénic regions, hence all MHD variables are ready for transferring from the inner-heliospheric model to the outer-heliospheric one straightforwardly. In our case, however, the plasma data are not provided from the MF model to the GHM model. If we place the interface (or upper boundary of the lower-corona MF model) in a sub-Alfvénic region at, for example,  $2.5 R_{\odot}$ , we may need additional assumptions for the physics quantities in order to obtain the desired coronal features at that height. For example, in Yeates & Mackay (2009), outward motions of the magnetic field are enforced on and near the upper boundary sphere at  $2.5 R_{\odot}$  to obtain a desired magnetic feature, the radial magnetic field structures in the outer corona. This upper-boundary treatment helps maintain an appropriate amount of the coronal magnetic field fluxes in the simulated corona with the evolving bottom-boundary solar-surface magnetic field, and yields long-term variations of the global coronal magnetic field structures successfully. However, the GHM model alone cannot numerically produce the closed-field coronal streamers or appropriate contrasts between the plasma quantities in the open-field and closed-field structures, if such outward flows are given all over the bottom-boundary interface surface set at  $2.5 R_{\odot}$ . To model the coronal plasma quantities from the time-evolving non-potential coronal magnetic field structures, it is required, or is at least a reasonable compromise, to fix the interface in the lower corona, in order to obtain reasonable structures of the (ambient) solar wind matching the magnetic structures derived from the MF model. In this study, we set the interface at the heliocentric distance of  $1.15 R_{\odot}$ , which is considered to be in a sub-Alfvénic region.

The second requirement is that the boundary treatment must be able to determine plasma quantities on the interface boundary in a self-consistent manner. The MF model can very robustly generate time-dependent three-dimensional coronal magnetic structures; however, it does not provide direct information about the plasma quantities necessary for the GHM model. Hence, a proper set of physical and mathematical assumptions must be introduced to the boundary treatment of the GHM models, such that the boundary plasma quantities can evolve consistently with the variations of magnetic field specified from the MF model and with the governing MHD equations.

To fulfill the second requirement, the GHM interface boundary treatment assumes and uses the concept of characteristics of the MHD equation system (e.g., Sauerwein 1966). The concept of the characteristics allows us to form a set of equations dictating temporal variations of the MHD variables on a boundary surface between two computation domains; hence, it is a powerful mathematical tool for constructing an interface boundary treatment at the  $r = 1.15 R_{\odot}$ , mostly sub-Alfvénic region. Without satisfying the mathematical concept, simulations may suffer from nonphysical, numerical vibrations on and near the sub-Alfvénic boundary surface sphere, and we will not be able to properly simulate the responses of the MHD variables in the upper

corona and interplanetary space to the time-varying magnetic field on the bottom-boundary sphere. In the present work, the boundary treatment is a modified version of the method of projected normal characteristics (Nakagawa et al. 1987; Wu & Wang 1987) that we used in our previous work (e.g., Hayashi 2005, 2013).

This paper is organized as follows: Section 2 briefly describes the MHD simulation schemes of the GHM. Section 3 provides details of the interface boundary treatment. Simulation procedures and results from a test simulation run, for a selected period of 2011 February, are given in Section 4. A summary and discussion are provided in Section 5.

## 2. Sun-to-Earth Global Heliospheric MHD Model (GHM)

The MHD simulation schemes used in this work are chiefly the same as in our earlier work, such as the total variant diminishing, the finite volume method, and the third-order MUSCL with the `minmod` flux limiting function (see Hayashi 2005, and references therein). The present model framework uses the Lax–Friedrichs method, instead of the Roe-type linearized Riemann solver, for speed. Temporal evolution of the MHD variables is traced with a two-step Runge–Kutta method.

With these methods in order to maintain computational stability in solving the nonlinear system with the second-order temporal and third-order spatial accuracies,  $\mathcal{O}((\Delta t)^2)$  and  $\mathcal{O}((\Delta x)^3)$ , the GHM module solves the temporal evolution of MHD variables governed by a set of compressible and ideal MHD equations,

$$\frac{\partial \varrho}{\partial t} = -\nabla \cdot (\varrho \mathbf{V}) \quad (1)$$

$$\begin{aligned} \frac{\partial (\varrho \mathbf{V})}{\partial t} = & -\nabla \cdot \left( P_g + \varrho \mathbf{V} : \mathbf{V} - \frac{1}{4\pi} \mathbf{B} : \mathbf{B} + \frac{B^2}{8\pi} \right) \\ & + \varrho (\mathbf{g} + (\boldsymbol{\Omega} \times \mathbf{r}) \times \boldsymbol{\Omega} + 2 \mathbf{V} \times \boldsymbol{\Omega}) \end{aligned} \quad (2)$$

$$\frac{\partial \mathbf{B}}{\partial t} = -\nabla \times \mathbf{E} \quad (3)$$

and

$$\begin{aligned} \frac{\partial \mathcal{E}}{\partial t} = & -\nabla \cdot \left[ \left( \frac{1}{2} \varrho V^2 + \frac{\gamma}{\gamma - 1} P_g \right) \mathbf{V} - \frac{1}{4\pi} (\mathbf{V} \times \mathbf{B}) \times \mathbf{B} \right] \\ & + \varrho \mathbf{V} \cdot (\mathbf{g} + (\boldsymbol{\Omega} \times \mathbf{r}) \times \boldsymbol{\Omega}), \end{aligned} \quad (4)$$

where  $t$ ,  $\varrho$ ,  $\mathbf{V}$ ,  $\mathbf{B}$ ,  $P_g$ ,  $\mathcal{E}$ , and  $\mathbf{g}$  are the time, mass density, velocity of plasma flow, magnetic field vector, gas pressure, total energy density ( $\varrho V^2/2 + P_g/(\gamma - 1) + B^2/8\pi$ ), and the solar gravitational force ( $-GM_{\odot}/r^3 \cdot \mathbf{r}$ ), respectively. The origin of the position vector ( $\mathbf{r}$ ) is the center of the Sun, and the plasma velocity ( $\mathbf{V}$ ) is evaluated in the frame rotating at the sidereal angular velocity ( $\boldsymbol{\Omega} = 14.23/\text{day}$ ). The electric field  $\mathbf{E}$  is calculated as  $(-\mathbf{V} \times \mathbf{B})$  except on and around the bottom-boundary sphere where it is specified from the MF model data as  $\mathbf{E} = -\partial_t \mathbf{A}$ . The colon ( $:$ ) denotes the dyadic product of two vectors. The specific heat ratio ( $\gamma$ ) of the polytropic approximation is assumed to be 1.05 and constant everywhere to mimic the near-isothermal situation of the solar corona and create the trans-Alfvénic solar wind (Parker 1958).

The spatial grid system is constructed in a spherical coordinate system. The angular cell size is constant at  $\pi/128$  in both the longitudinal and latitudinal directions, which matches the grid system of the lower-corona MF simulation. At and near the north pole ( $\theta \sim 0$ ) and the south pole ( $\theta \sim \pi$ ), the simulated primitive variables are averaged over power-of-two cells in the longitudinal direction in order to mitigate the severe Courant–Friedrich–Levy (CFL) condition imposed on the time step size ( $\Delta t$ ) (Hayashi 2008). In the radial direction a total of 145 grid cells cover the range of heliocentric distance from the interface sphere at  $1.15 R_{\odot}$  to about 1 au, with the grid cell size ( $\Delta r$ ) gradually increasing from  $\Delta r = 0.01672 R_{\odot}$  on the bottom interface boundary sphere to about  $3 R_{\odot}$  at 1 au.

### 3. GHM-MF Interface Boundary Treatment

Our earlier model for the global solar corona and solar wind (Hayashi 2005, 2008) is originally designed for simulating coronal regions from the solar surface, set at 1 or  $1.01 R_s$ , so that the solar-surface magnetic field data (such as those in the synoptic map format, e.g., Liu et al. 2017) can be directly used as the boundary condition. In this earlier model, the projected normal characteristics method (Nakagawa et al. 1987; Wu & Wang 1987; Hayashi 2005) is applied to reduce unphysical oscillations on and near the sub-Alfvénic boundary sphere. A later version of our global MHD model (Hayashi 2013) achieves the capability of introducing temporal evolution of the radial component of the observed solar-surface magnetic field as time-varying boundary values. We have recently developed another type of data-driven MHD model for a local, active region (AR; Hayashi et al. 2018, 2019). In this AR data-driven MHD model, temporal variations of all three magnetic field components are fully introduced as the curls of three electric field vectors that are derived through three Poisson equations (hence, named as the Surface Electric field Estimated with 3 Poisson solvers, SEE3Po; Hayashi et al. 2018, 2019).

In the present GHM model, all three components of magnetic field and their temporal derivatives on the interface boundary sphere are specified as the curl of the vector potential and their temporal derivatives, as  $\mathbf{B} = \nabla \times \mathbf{A}$  and  $\partial_t \mathbf{B} = -\nabla \times \mathbf{E} = \nabla \times (\partial_t \mathbf{A})$ , given from the MF model. Our provisional simulations, however, suggested that fully obeying the given  $\mathbf{B}$  often causes numerical instability. For example, near-radial plasma flows at the coronal-hole bases may change abruptly in response to a sudden increase of the horizontal magnetic field. The MF model uses the pseudo plasma flow vector assumed to be parallel to the local Lorentz force,  $\mathbf{V} \propto \mathbf{J} \times \mathbf{B}$ , but we cannot use this pseudo-velocity as  $\mathbf{V}$  is always perpendicular to  $\mathbf{B}$ . To achieve computational stability, the interface boundary treatment in the GHM calculates the temporal variations of the plasma quantities on the GHM bottom boundary using the projected normal characteristics method.

#### 3.1. Magnetic and Electric Field Vectors on and around the Interface Sphere

The MF model simulates the temporal variations of the vector potential,  $\mathbf{A}$ , in the lower corona, which the GHM uses to determine the initial magnetic field distribution (at  $t = 0$ ), as  $\mathbf{B} = \nabla \times \mathbf{A}$ , and the electric field (at  $t \geq 0$ ), as  $\mathbf{E} = -\partial_t \mathbf{A}$ , to drive the simulated system. The HMI vector magnetic field data are used to determine the initial three-dimensional magnetic

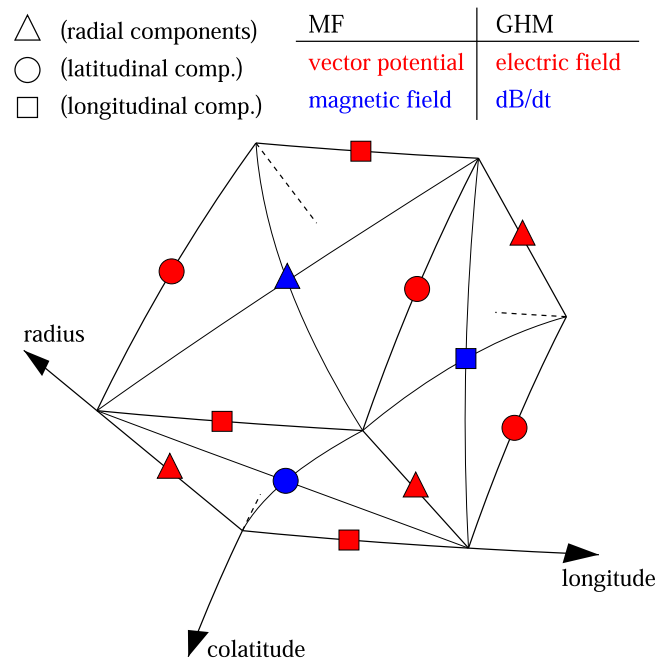


**Figure 1.** The vector quantities of the MF and GHM models in the staggered Yee grid system. The vector potential  $\mathbf{A}$  (the magnetic field vector  $\mathbf{B}$ ) of the MF model is defined at the edge centers (face centers) and marked with red-filled (blue-filled) marks in this diagram. In the GHM model, each component of the electric field on the edges is calculated as  $E_{r,\theta,\phi} = -\partial_t A_{r,\theta,\phi}$ , and the temporal variations of the magnetic field at the face center are calculated as  $\partial_t \mathbf{B} = -\nabla \times \mathbf{E}$ . The fluxes of these curl products (or the line integrals along edges) are interpolated to determine the values of  $\mathbf{B}$  and  $\partial_t \mathbf{B}$  at the cell center, which is not drawn in this plot. Three different shapes of marks represent the components of vector quantities. A pair of diagonal curves are drawn on each visible face to indicate its face center. Only the visible side in perspective is drawn, except parts of edges at the back side drawn with dashed lines.

field configuration of the MF model through the method described in Section 4 of Hoeksema et al. (2020). Estimations of  $\mathbf{B}$  and  $\mathbf{E}$  involve temporal and spatial interpolations because the two models use different data file recording practices and different differencing methods.

In the current framework, the MF model records the magnetic field quantities every 2000 simulation time step counts. Because the MF simulation time step varies in accordance with the CFL condition, the physical time intervals between two data files range from 5 to 10 hr. On the other hand, the GHM model assumes data files are stored with a constant physical time interval of, for example, 0.2 days. Hence, a preprocessing step is needed to reorganize the MF data to account for the difference, and the GHM uses the reorganized data to calculate the temporal derivatives of the vector potential,  $\partial_t \mathbf{A}$ . Although the temporal interpolation process introduces some error, the error does not cause a large amplitude of differences in the derived  $\mathbf{B}$  from the original values of the MF data.

The MF model uses the Yee-mesh system (Yee 1966) and provides the magnetic field component normal to the cell face at the face center and the vector potential and electric field on the edges. Figure 1 shows the positions in a computational cell to which the physical vector variables are assigned. The GHM model requires numerical fluxes at the face centers to calculate temporal derivatives of the MHD variables at the cell centers. To adjust the differences in the positions, spatial interpolations are applied. From  $\mathbf{A}$  ( $\mathbf{E} = -\partial_t \mathbf{A}$ ) at the edge centers (shown with red-filled marks),  $\mathbf{B}$  ( $\partial_t \mathbf{B}$ ) at the face centers (with

blue-filled marks) are calculated with an ordinary curl operation, the line integral along edges divided by the area of the cell face. Each component of  $\mathbf{B}$  and  $\partial_r \mathbf{B}$  at the cell center is calculated as the average of the two line integrals (equal to the total flux over the face) on the faces whose normal corresponds to the vector component, then divided by the area of the section containing the cell center.

The MF model does not cover the regions within about  $17^\circ$  from the north and south poles of the solar surface. The current GHM part fills the bottom-boundary surface near the poles with the average value of  $B_r$  of the nearest available data points, and zero values for  $B_\theta$  and  $B_\phi$ . No specific adjustments are made to the electric field at the limit boundaries of the MF area coverage, because the curl of this unadjusted  $\mathbf{E}$  did not cause unphysically large magnitudes of the magnetic field.

### 3.2. Projected Normal Characteristics Method

The boundary treatment will determine the temporal variations of these quantities on the interface boundary sphere in accordance with the concept of the characteristic. In our earlier work (Hayashi 2013), where only the distribution of  $B_r$  and its temporal variation are specified, we can solve the temporal variations of the other MHD variables simultaneously. However, in this case, the GHM has all three components of the magnetic field and their temporal variations specified; hence, we need to modify the existing boundary treatments. In brief, we split the simulation updating procedure into two stages.

In the first stage, the MHD variables are updated as if the temporal variations of the bottom-boundary magnetic field are equal to zero. We use the choice labeled Case O in Hayashi (2005), in which two different sets of characteristics relationships are applied depending on the value of the radial component of the plasma flow,  $V_r$ . The first relationship for  $V_r \sim 0$  is typically in the bottom-boundary regions of stagnant plasma at the base of closed-field coronal streamers, and the second for  $V_r > 0$  in the base of open-field coronal holes.

In the second stage, the specified temporal variation of bottom-boundary magnetic field  $\Delta \mathbf{B}$  is added to the simulated  $\mathbf{B}$ , and the other MHD variables (plasma quantities and total energy density) evolve following a new set of the characteristics equations. Practical forms of the new set of characteristics equations and calculation steps are given in the Appendix.

In the first stage, the two horizontal components of the boundary magnetic field ( $B_\theta$  and  $B_\phi$ ) can be altered. Among the possible choices we examined, this is likely the best alternative for maintaining numerical stability and achieving the capability for tracing the given temporal variations of the boundary magnetic field with reasonable accuracy.

### 3.3. Boundary Magnetic Field Derived through Interface Treatments

As described in previous sections, there are several occasions in the GHM simulation model at which the horizontal components of the simulated bottom-boundary magnetic field can deviate from those given by the MF model. These occasions include linear interpolation, errors in the discretized schemes, and the characteristic-based boundary treatments. In particular, the characteristic-based boundary treatment specifically deals with the nonlinear MHD interaction between the boundary surface and the computation domain above the

surface, and hence, the derived temporal variations cannot be predicted. As such, it is possible that the differences grow unacceptably large in time.

Figure 2 compares the bottom-boundary magnetic field of the GHM with the magnetic field of the MF model at the same height at  $t = +3d$ . Except at the northern and southern limits of the MF model areal coverage, the differences are moderately small. One of the factors expected to be a likely cause of the differences is the boundary treatment for the regions with  $V_r > 0$  (corresponding to the base of a coronal hole). Fortunately, we do not see significantly large differences in the regions with  $V_r > 0$  (shown in the top row). This is probably because the regions corresponding to the coronal-hole bases tend to have a predominantly radial magnetic field with relatively small horizontal components both in the GHM and MF models. Instead, a few regions with large differences are found around the coronal-hole bases. These regions are at outer parts of the previously closed-field regions (corresponding to the coronal streamers), and the horizontal components in such regions are more likely affected by the variations of the global magnetic field distribution and by the interactions between the open-field coronal holes and the closed-field coronal streamers.

The scatter plots in Figure 3 compare the two magnetic field maps qualitatively. The area-weighted correlation coefficient for  $B_r$  is about 1.0, and that of the two horizontal components is about 0.7. The slope and intercept of the linear regression are close to 1 and 0 for the three components. The average absolute differences in  $B_\theta$  and  $B_\phi$  are about 0.2 Gauss, within 10% of the original MF data. These numbers suggest that our boundary treatment reasonably reproduces the given temporal variations of magnetic field; hence we believe that the simulated responses of the solar corona and solar wind to the given variation are reasonable.

## 4. Simulation and Results

The GHM simulation consists of two parts. In the first part, the time-relaxation simulation is performed starting with the initial three-dimensional magnetic field configuration obtained through the potential-field source-surface model (PFSS model; Altschuler & Newkirk 1969; Schatten et al. 1969) using a  $B_r$  map at  $t = 0$  from the MF data at  $r = 1.15 R_\odot$ . In the second part, the relaxed state is driven with the time-dependent electric field  $\mathbf{E} = -\partial_t \mathbf{A}$  from the MF model.

Figures 4 and 5 show the magnetic field lines obtained through the two parts of the GHM simulation. The initial PFSS magnetic field in the relaxation simulation is shown in plot (a). The initial plasma flow is the trans-Alfvénic near-isothermal polytropic plasma flow (the Parker solution; Parker 1958), with the plasma flow on the inner boundary sphere adjusted to be parallel to the magnetic field,  $\mathbf{V} := (V_r B_r / B^2) \mathbf{B}$ . With  $B_r$  fixed all through the relaxation simulation, the simulated system will reach a relaxed, quasi-steady state matching the global boundary distribution of  $B_r$  (plot (b)). With the current simulation setting (i.e., the temperature at the critical radius of the initial Parker solution at  $r \sim 5.5 R_\odot$  of 1.0 MK), one relaxation simulation typically takes the physical time of about 50 hr until the simulated system reaches a (quasi-)steady state for  $r < 50 R_\odot$ , or about 5 to 7 days for  $r < 1$  au.

The relaxed state obtained through the first simulation is used as the initial condition in the second data-driven simulation, in which the relaxed (quasi-)steady state is driven by the time-dependent three-component boundary magnetic

plasma flow and magnetic field at interface height,  $r = 1.15R_s$ ,  $t = +3.0d$

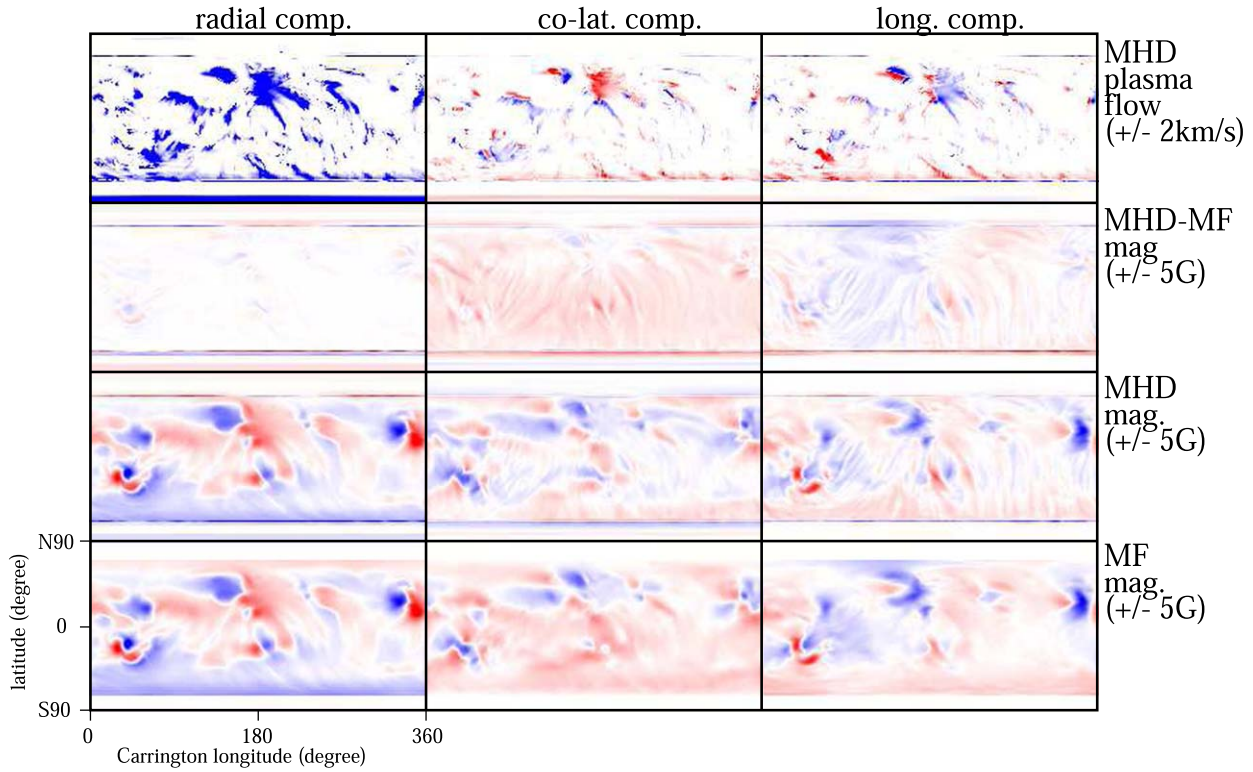


**Figure 2.** Latitude–longitude maps of bottom-boundary variables, at  $t = +3d$ . From left to right, the radial, colatitudinal, and longitudinal components of four vector quantities of (from bottom) the magnetic field in the MF model, the bottom-boundary magnetic field of the GHM MHD model, and the differences of the magnetic field between the MHD model and the MF model, and the simulated bottom-boundary plasma velocity, are shown. Positive (negative) values are presented with blue (red) colors, truncated at the values in the right side of the plots. Anomalous values near the top and bottom of each plot are caused through the treatments of the boundaries of the MF area coverage.

Interface Magnetic Field, at  $1.15R_s$   
area-weighted scatter plot; at  $t = +3.0 d$

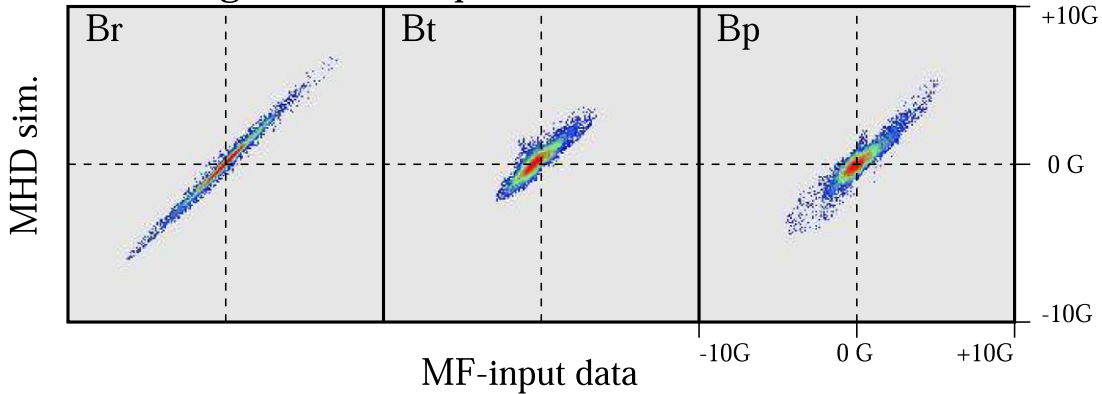


**Figure 3.** Scatter plots of the magnetic field components between the MF data at  $1.15 R_\odot$  and the bottom-boundary values in the GHM simulation; from left, the radial, latitudinal, and longitudinal components at  $t = +3d$ . Colors represent the area-weighted scatter density, counted with a bin size of  $0.1G$ , in a logarithm scale. Red, green, and blue colors are for the scatter densities,  $10^2$ ,  $10^1$ , and  $10^0$  in units of  $4\pi/10^4$  sr, respectively. The near-pole areas that the MF model does not cover are not included in generating these plots.

field. Plots (c) and (d) in Figures 4 and 5 exhibit an example of the obtained coronal magnetic field variations. The GHM simulation can numerically produce twisted nonpotential magnetic field structures, just as the MF model does for the lower corona. It can also numerically produce eruptions, or sudden outward motions, of twisted magnetic field structures. One such eruption is found in the region above a newly emerging solar active region (NOAA 11158) that is taken into

account in the data-assimilation process in the MF model. Figure 6 offers another demonstration of the erupting magnetic field structure.

The eruption of the magnetic structure is accompanied by compression of the coronal plasma in the vicinity. Figure 7 shows the propagation of a shell-shaped density enhancement caused by the magnetic eruption event shown in Figure 6. An advantage of compressible MHD models is the capability of

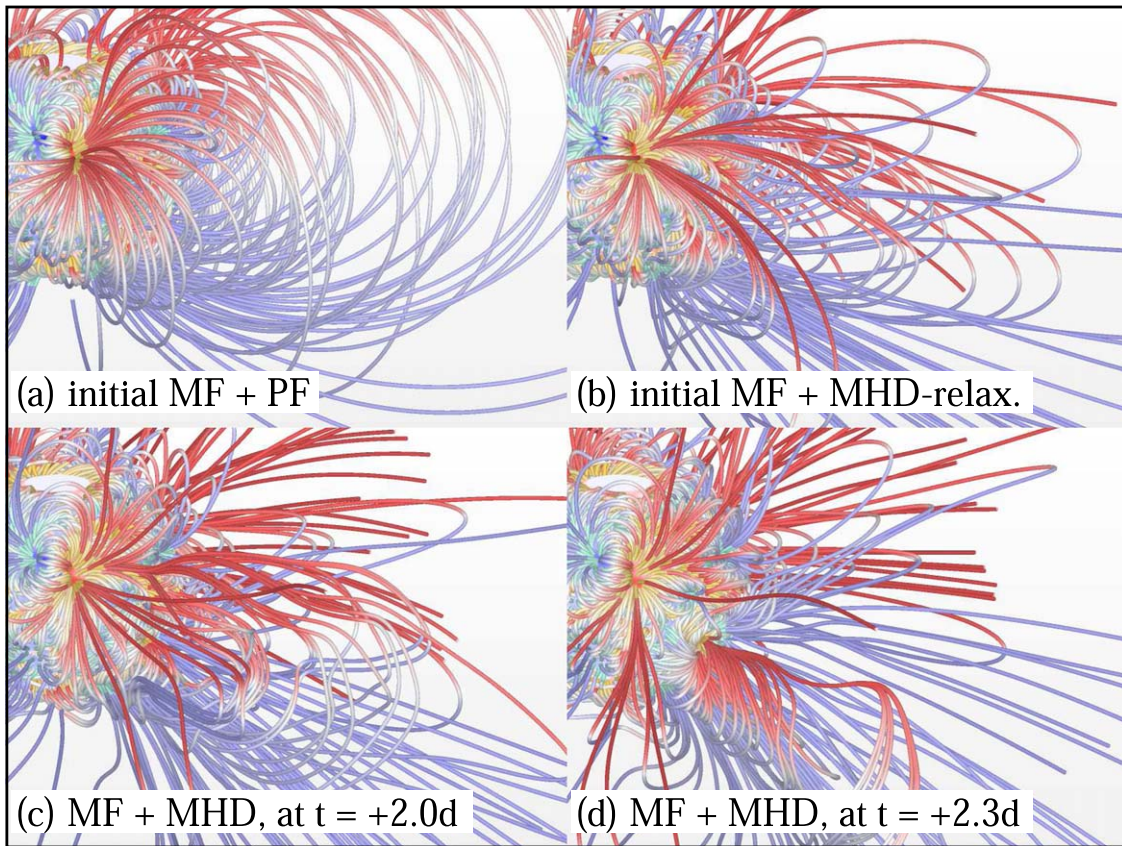


**Figure 4.** Snapshots of the coronal magnetic field lines, viewed from the direction of 340 Carrington longitude degrees and 15 degrees latitude north at selected computation parts and simulation instants: (a) the potential-field configuration as the initial value of time-relaxation simulation (first simulation part), (b) the MHD-relaxed state, (c) the data-driven state at  $t = +2d$  in the second simulation part, and (d) the data-driven state at  $t = +2.3d$ . In the lowermost corona at  $r \leq 1.15 R_{\odot}$ , the field line segments with positive (negative)  $B_r$  are colored with cyan (yellow). At  $r \geq 1.15 R_{\odot}$ , the blue and red colors are, respectively, indicating positive and negative  $B_r$  polarity of the magnetic field.

simulating the evolution of plasma quantities. This density enhancement propagates at a speed just about  $50 \text{ km s}^{-1}$  greater than surrounding coronal plasma flows. This rather slow motion is in part due to the polytropic assumption. The plasma at  $r < 5 R_{\odot}$  is not well accelerated to reach Alfvén speed, hence the plasma density (which roughly obeys the mass-flux conservation law,  $\rho V_r \sim \text{const.}$ ) is much higher than in the actual corona.

## 5. Summary and Discussion

In this paper the methodology of the GHM model and its interface boundary treatment with the lower coronal magneto-friction model are provided, and the results from a test simulation for a selected period (2011 February) are presented.

As seen in Figures 4 and 5, several nonpotential twisting structures of the coronal magnetic field are numerically reproduced. As a consequence of increases of the nonpotentiality (or magnetic pressure, or magnetic energy density), eruption events are numerically reproduced (Figure 6). Simulation of such eruption events in a data-driven physics-based manner demonstrates the new capability the CGEM project aims at. It should be noted, however, that this particular simulated eruption event does not correspond to any actual event observed within a few days of the simulated eruption time. The present model is not yet ready for operational use or space-weather purposes. Nonetheless, we would emphasize that the presented model combination can be a key piece of a

model framework aimed toward the more powerful capability of data-driven modeling of enigmatic nonlinear processes in the solar corona, solar wind, and heliosphere.

Several aspects of the GHM model still need improvement. The present GHM model assumes a polytropic plasma with specific heat ratio close to 1, which is a widely used assumption in solar-corona simulations. However, this assumption should be replaced with more physics-based coronal heating/acceleration models such as those shown in Usmanov et al. (2011) and Feng et al. (2017). For simplicity magnetic diffusivity is not included in the governing equations in the current stage of our effort, but this must be included in the future, as magnetic reconnection is a key process for reproducing coronal energetic events.

The mathematical concept employed in this work properly handles physical information propagating from one side of the interface to the other, and in principle can handle information propagating in the other direction as well. The RADMHD model can simulate the low corona in a more physical way than the MF approach, but it is much more computationally expensive, particularly when extending the model over global spatial scales. Yet there are significant advantages of coupling two global dynamic models. One such advantage is the possibility of a two-way interface coupling in which the characteristic-based methods will sort the MHD wave modes (or information associated with the wave modes) maintaining consistency in physics in both models.

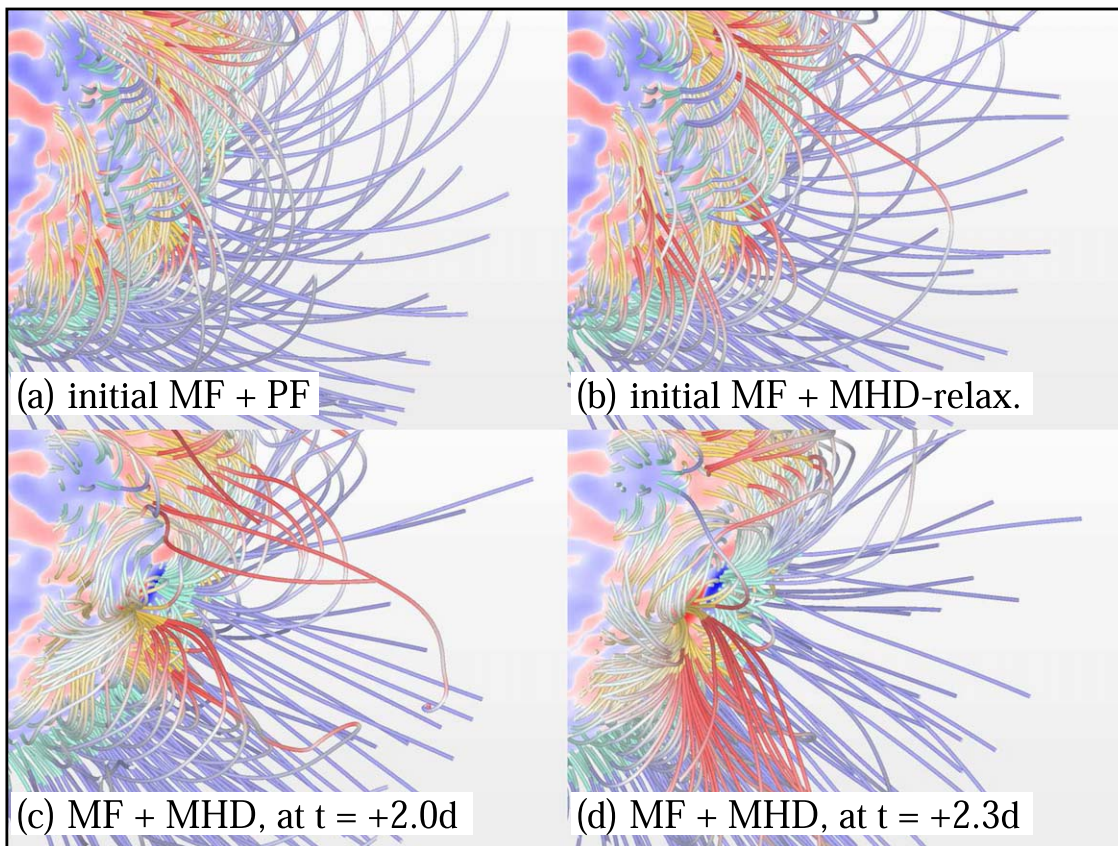


**Figure 5.** Same as in Figure 4 except that only the field lines at a lower coronal volume ( $r \leq 2 R_{\odot}$ ) are drawn. The field lines within 45 longitude degrees from the view point are omitted, for better visibility of a newly emerging solar active region (AR 11158) whose polarity pair is visible in (c) and (d).

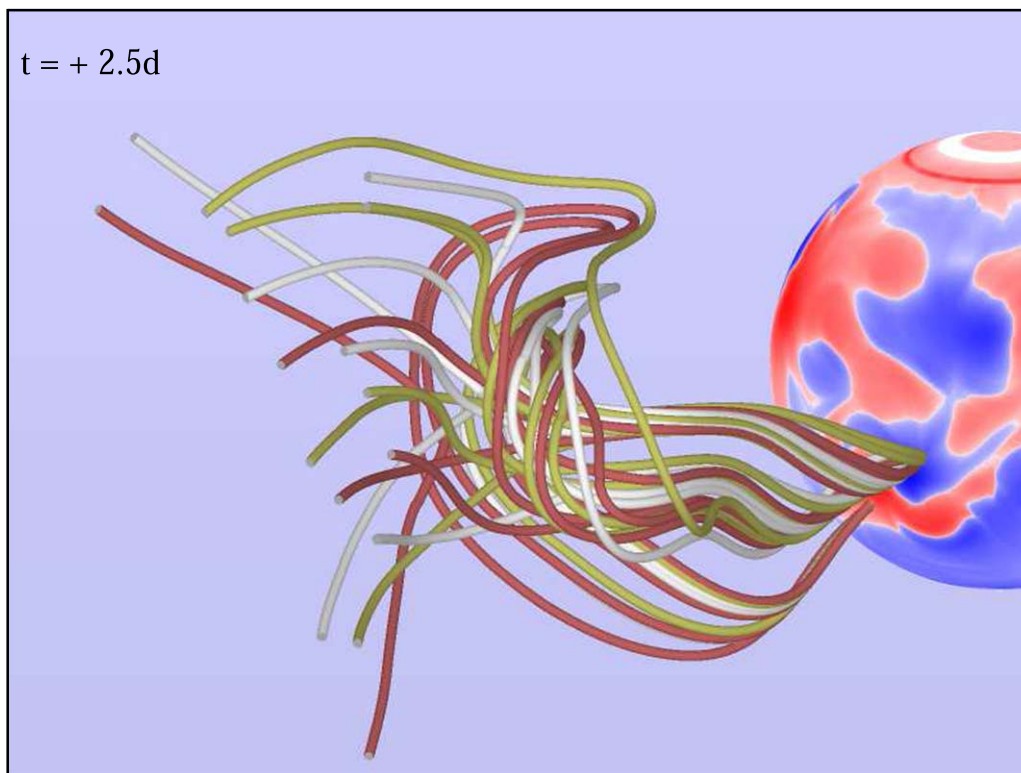


**Figure 6.** Selected field lines demonstrating an erupting twisted magnetic field structure, above a large active region (AR 11158). The colors on the sphere shows the boundary  $B_r$  on the interface boundary sphere at  $1.15 R_{\odot}$  (blue for positive polarity and red for negative polarity).

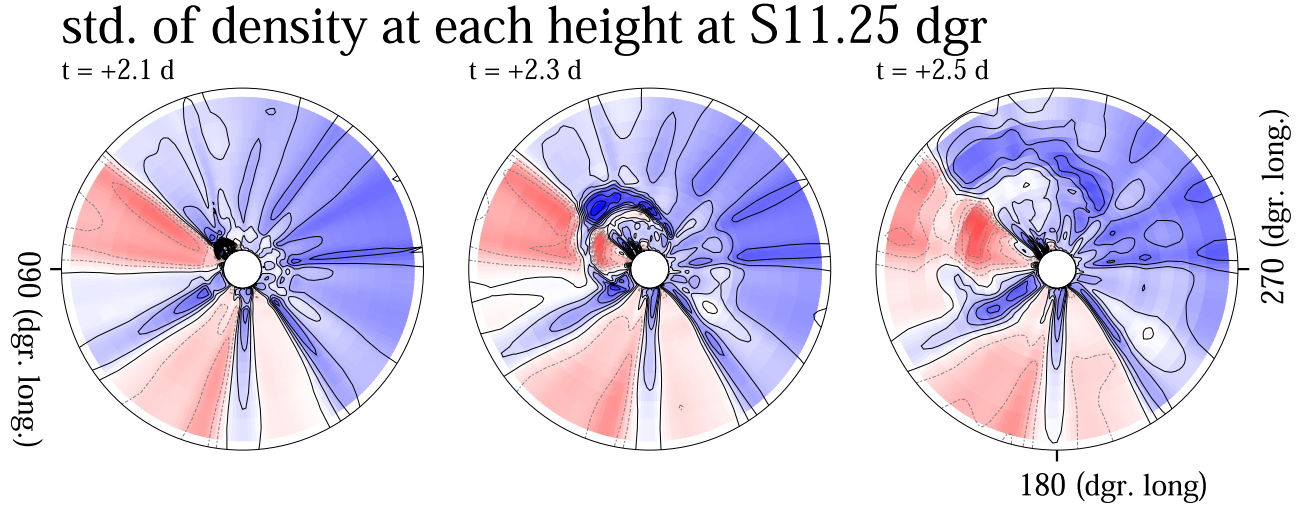


**Figure 7.** The standard deviations of the simulated plasma density calculated at each height from 1.15 to 11  $R_{\odot}$ , on a cone surface at 11°25 south latitude, at  $t = +2.1$ ,  $+2.3$ , and  $+2.5d$ . The regions with higher (lower) density than the average at each height are colored with blue (red), superimposed with contour lines placed at a fixed interval of 0.5 standard deviation level. A shell-shaped density enhancement, associated with the eruption of twisted magnetic field structure shown in Figure 6, starts propagating outward from around 20° of Carrington longitude.

It is also possible to construct a one-way interface, from RADMHD to GHM, in which the GHM bottom-boundary variables will fully follow the outputs from RADMHD without using the characteristic-based boundary treatments, as RADMHD will provide all eight MHD variables. In this case, the vertical gradients of the MHD variables will be a key piece of information to be passed from the RADMHD to the GHM; because information of the physical state at a single height is not sufficient for the GHM to simulate the upper corona and solar wind in a physically consistent manner such that, for example, the divergence-free condition can be maintained properly. Although there are some difficulties anticipated in coupling the RADMHD and GHM models, such as those arising from the difference in the specific heat ratio (5/3 in the RADMHD and 1.05 in the GHM), potential benefits of such a new model coupling could be substantial.

The authors appreciate the anonymous referee for constructive comments and suggestions that helped improve this article. This work was supported by NASA and NSF through their funding of the CGEM project, through NSF award AGS-1321474 to UC Berkeley, NASA award 80NSSC18K0024 to Lockheed Martin, and NASA award NNX13AK39G and contract NAS5-02139 (HMI) to Stanford University. This work was also supported by NASA through the one-year extension to the CGEM project, ECGEM, through award 80NSSC19K0622 to UC Berkeley. We used the SDO/HMI data through the courtesy of NASA and the SDO science teams. Some of the simulations were conducted on the supercomputer system “Flow” at Nagoya University, through the computational joint research program of the Institute for Space-Earth Environment Research, Nagoya University, Japan.

## Appendix

### A Characteristic-based Method with Magnetic Field Addition

In the concept of characteristics, the number of constraints given on temporal variations of MHD variables on a boundary surface must be equal to the number of MHD waves incoming (in the global solar-corona model, the incoming waves are

those directing outward from the Sun). In the case of the GHM-MF interface, in general, the number of incoming waves is five or six; hence, we have to give six constraints.

Let us consider a time step from  $t^n$  to  $t^{n+1}$  ( $= t^n + \Delta t$ ; the superscripts,  $n$  and  $n + 1$  are time step counts). We give three constraints by specifying arbitrary temporal variations of the magnetic field,  $\Delta \mathbf{B} (= \mathbf{B}^{n+1} - \mathbf{B}^n)$ . Another two constraints are given by assuming that the simulated plasma flow is parallel to the local magnetic field at the two instants,  $\mathbf{V}^n \parallel \mathbf{B}^n$  and  $\mathbf{V}^{n+1} \parallel \mathbf{B}^{n+1}$ . It must be noted that this condition does not always hold. For example, in a horizontal magnetic flux tube moving radially away from the Sun, the plasma motion vector is not parallel to the magnetic field vector. Nonetheless, this is the best choice among possible choices we had tested.

Letting  $\Delta X$  be a variation of a variable  $X$  over time  $\Delta t (= t^{n+1} - t^n)$  and writing the temporal variation of  $X$  over the time step  $\Delta t$  as  $X^{n+1} = X^n + \Delta X$ , the parallel condition ( $\mathbf{V} \times \mathbf{B} = \mathbf{0}$ ) yields  $V_{\theta, \phi}^n B_r^n - V_r^n B_{\theta, \phi}^n = 0$  and  $V_{\theta, \phi}^{n+1} B_r^{n+1} - V_r^{n+1} B_{\theta, \phi}^{n+1} = 0$ , leading to two constraint relationships,

$$B_r \Delta V_{\theta, \phi} + V_{\theta, \phi} \Delta B_r - B_{\theta, \phi} \Delta V_r - V_r \Delta B_{\theta, \phi} = 0 \quad (\text{A1})$$

after disregarding the second-order differences.

Imposing the parallel condition with the given  $\Delta \mathbf{B}$  is equivalent to discarding the Alfvén wave mode. Therefore, in the current GHM model, only two outgoing compressible MHD wave modes (i.e., the fast and slow modes) are considered in constructing the characteristic-based boundary treatment for the second stage of the two-step updating procedure. Here we note that the first stage of the two-step updating procedure considers the Alfvén wave mode; therefore, the Alfvén mode wave is taken into account through the two-stage updating procedure as a whole.

From the polytropic relationship, which is also applied in the governing equations,

$$\left[ \frac{\partial}{\partial t} + \mathbf{v} \cdot \nabla \right] \left( \frac{P_g}{\varrho^{\gamma}} \right) = 0, \quad (\text{A2})$$

the last sixth constraint is given as

$$\Delta P_g = \frac{\gamma P_g}{\varrho} \Delta \varrho. \quad (\text{A3})$$

By combining the six constraints above, we can rewrite the characteristics equations for the fast and slow modes as

$$\begin{aligned} & \left[ L_{1l} + \left( \frac{\gamma P_g}{(\gamma - 1)\varrho} - \frac{v_r^2 + v_\theta^2 + v_\phi^2}{2} \right) L_{7l} \right] \Delta \varrho \\ & + \left[ \frac{B_r L_{2l} + B_\theta L_{3l} + B_\phi L_{4l}}{B_r} \right. \\ & \left. + \frac{V_r B_r + V_\theta B_\theta + V_\phi B_\phi}{B_r} L_{7l} \right] \Delta(\varrho V_r) \\ & = \frac{L_{3l}}{B_r} (\varrho V_\theta \Delta B_r - \varrho V_r \Delta B_\theta) \\ & + \frac{L_{4l}}{B_r} (\varrho V_\phi \Delta B_r - \varrho V_r \Delta B_\phi) \\ & - L_{5l} \Delta B_\theta - L_{6l} \Delta B_\phi \\ & - \left[ \frac{B_r^2 - \varrho (V_\theta^2 + V_\phi^2)}{B_r} \Delta B_r \right. \\ & \left. + \frac{B_r B_\theta + \varrho V_r V_\theta}{B_r} \Delta B_\theta \right. \\ & \left. + \frac{B_r B_\phi + \varrho V_r V_\phi}{B_r} \Delta B_\phi \right] L_{7l}, \quad (\text{A4}) \end{aligned}$$

where  $L_{ml}$  is the element of left eigen matrix of the MHD equation system,  $\mathbf{L}$  (Cargo & Gallice 1997; Hayashi 2005), with a subscript  $m$  for indicating the  $m$ th MHD variables, and  $l$  for the  $l$ th MHD wave mode. In a convention (Hayashi 2005),  $m$  runs from 1 to 7 for  $\varrho, \varrho V_r, \varrho V_\theta, \varrho V_\phi, \varrho B_\theta, \varrho B_\phi$ , and  $\mathcal{E}$ , and  $l$  runs from 1 to 7 for the wave modes with the eigenvalues (or wave mode speed) of  $V_r - V_f$ ,  $V_r - V_A$ ,  $V_r - V_s$ ,  $V_r$ ,  $V_r + V_s$ ,  $V_r + V_A$ ,  $V_r + V_f$  (here,  $V_f$ ,  $V_A$ , and  $V_s$  are the fast, Alfvén, and slow mode speeds, respectively, in the radial direction or the normal to the boundary surface, respectively).

Equation set (A4) consists of two equations ( $l=5$  for the outgoing slow mode and  $l=7$  for the outgoing fast mode) with two unknown variables. The temporal variations of magnetic field ( $\Delta \mathbf{B}$ ) appearing at the right-hand side are all given and known, and the two unknown variables,  $\Delta \varrho$  and  $\Delta(\varrho V_r)$ , at the left-hand side can be determined. This two-equation set is always solvable, except when  $|B_r| \sim 0$ ,  $\varrho \sim 0$ , or  $P_g \sim 0$ . The other remaining temporal variations,  $\Delta(\varrho V_\theta)$ ,  $\Delta(\varrho V_\phi)$ , and  $\Delta P_g$  (or  $\Delta \mathcal{E}$ ), are calculated through Equations (A1) and (A3). Notice that the derived temporal variations are all zero when  $\Delta \mathbf{B} = \mathbf{0}$  (for example, in the time-relaxation simulation).

The equation set (A4) has  $B_r$  at the denominator, hence it is not applicable for regions on or close to the polarity inversion lines or magnetically neutral lines where  $|B_r|/|B|$  is small. For such horizontal-field regions, another characteristic-based boundary condition labeled as BC0 in Hayashi (2005), which handles stagnant-plasma regions ( $V_r = 0$ ), is applied.

## ORCID iDs

Keiji Hayashi  <https://orcid.org/0000-0001-9046-6688>  
 William P. Abbett  <https://orcid.org/0000-0003-3961-2381>  
 Mark C. M. Cheung  <https://orcid.org/0000-0003-2110-9753>  
 George H. Fisher  <https://orcid.org/0000-0002-6912-5704>

## References

- Abbett, W. 2007, *ApJ*, **665**, 1469  
 Abbett, W. P., & Bercik, D. J. 2014, AAS Meeting, **224**, 123.47  
 Abbett, W. P., & Fisher, G. H. 2012, *SoPh*, **277**, 3  
 Altschuler, M. D., & Newkirk, G., Jr. 1969, *SoPh*, **9**, 131  
 Cargo, P., & Gallice, G. 1997, *JCoPh*, **136**, 446  
 Cheung, M. C. M., & DeRosa, M. L. 2012, *ApJ*, **757**, 147  
 Craig, I. J. D., & Sneyd, A. D. 1986, *ApJ*, **311**, 451  
 Dettman, T. R., Intriligator, D. S., Dryer, M., et al. 2011, *JGRA*, **116**, A03105  
 Dryer, M., Smith, K., Coates, A. J., & Johnstone, A. D. 1991, *SoPh*, **132**, 353  
 Feng, X., Ma, X., & Xiang, C. 2015, *JGRA*, **120**, 10159  
 Feng, X. S., Li, C., Xiang, C., et al. 2017, *ApJS*, **233**, 10  
 Feng, X. S., Yang, L., Xiang, C., et al. 2010, *ApJ*, **723**, 300  
 Fisher, G. H., Kazachenko, M. D., Welsch, B. T., et al. 2020, *ApJS*, **248**, 2  
 Fisher, G. H., Abbett, W. P., Dercik, D. J., et al. 2015, *SpWea*, **13**, 369  
 Hayashi, K. 2005, *ApJS*, **161**, 480  
 Hayashi, K. 2008, *JGRA*, **113**, A07104  
 Hayashi, K. 2012, *JGRA*, **117**, A08105  
 Hayashi, K., Feng, X., Ming, X., & Jiang, C. 2018, *ApJ*, **855**, 11  
 Hayashi, K., Feng, X., Ming, X., & Jiang, C. 2019, *ApJL*, **871**, L28  
 Hayashi, K., Hoeksema, J. T., Liu, Y., et al. 2015, *SoPh*, **290**, 1507  
 Hayashi, K. 2013, *JGRA*, **118**, 6889  
 Hinterreiter, J., Magdalenic, J., Temmer, M., Verbeke, C., et al. 2019, *SoPh*, **294**, 170  
 Hoeksema, J. T., Abbett, W. P., Bercik, D., Cheung, M. C. M., et al. 2020, *ApJS*, **250**, 28  
 Hoeksema, J. T., Liu, Y., Hayashi, K., Sun, X., et al. 2014, *SoPh*, **289**, 3483  
 Jin, M., Manchester, W. B., van der Holst, B., Sokolov, I., Tóth, G., et al. 2017, *ApJ*, **834**, 173  
 Kazachenko, M. D., Fisher, G. H., & Welsch, T. 2014, *ApJ*, **795**, 17  
 Li, H., Feng, X., Zuo, P., & Wei, F. 2020, *ApJ*, **900**, 76  
 Linker, J. A., Mikić, Z., Biesecker, D. A., et al. 1999, *JGR*, **104**, 9809  
 Linker, J. A., van Hoven, G., & Schnack, D. D. 1990, *GeoRL*, **17**, 2281  
 Liu, Y., Hoeksema, J. T., Sun, X., & Hayashi, K. 2017, *SoPh*, **292**, 29  
 Merkin, V. G., Lionello, R., Lyon, J. G., et al. 2016, *ApJ*, **831**, 23  
 Nakagawa, Y., Hu, Y. Q., & Wu, S. T. 1987, *A&A*, **197**, 354  
 Odstrcil, D., & Pizzo, V. J. 1999, *JGR*, **104**, 28225  
 Odstrcil, D., & Pizzo, V. J. 2009, *SoPh*, **259**, 297  
 Parker, E. N. 1958, *ApJ*, **128**, 664  
 Pogano, P., Mackay, D. H., & Yeates, A. R. 2018, *JSWSC*, **8**, 26  
 Pogorelov, N. V., Heenkhuizen, J., Roytershteyn, V., et al. 2017, *ApJ*, **845**, 9  
 Pomoell, J., & Poedts, S. 2018, *JSWSC*, **8**, 35  
 Riley, P., Lionello, R., Linker, J. A., et al. 2011, *SoPh*, **274**, 361  
 Sauerwein, H. 1966, *JFM*, **25**, 17  
 Schatten, K. H., Wilcox, J. M., & Ness, N. F. 1969, *SoPh*, **6**, 442  
 Scherrer, P. H., Schou, J., Bush, R. I., et al. 2012, *SoPh*, **275**, 207  
 Shen, F., Wang, Y., Feng, X., & Xiong, C. 2013, *GeoRL*, **40**, 1457  
 Shiota, D., & Kataoka, R. 2016, *SpWea*, **14**, 56  
 Steinolfson, R. S., Suess, S. T., & Wu, S. T. 1982, *ApJ*, **255**, 730  
 Usmanov, A. V. 1993, *SoPh*, **148**, 371  
 Usmanov, A. V., Matthaeus, W. H., Breech, B. A., & Goldstein, M. L. 2011, *ApJ*, **727**, 84  
 van Ballegoijen, A. A., Priest, E. R., & Mackay, D. H. 2000, *ApJ*, **539**, 983  
 Wu, C.-C., Dryer, W. S. T., Wood, B. E., et al. 2011, *JGRA*, **116**, A12103  
 Wu, S. T., & Wang, J. F. 1987, *CMAME*, **64**, 267  
 Xiong, M., Davies, J. A., Harrison, R. A., et al. 2018, *ApJ*, **852**, 111  
 Yang, W. H., Sturrock, P. A., & Antiochos, S. K. 1986, *ApJ*, **309**, 383  
 Yeates, A. R., & Mackay, D. H. 2009, *ApJ*, **699**, 1024  
 Yee, K. 1966, *ITAP*, **14**, 302